Nanoscale Advances

ROYAL SOCIETY OF CHEMISTRY

PAPER

View Article Online
View Journal | View Issue

Cite this: *Nanoscale Adv.*, 2021, **3**, 812

Direct Z-scheme α-MnO_2@$MnIn_2S_4$ hierarchical photocatalysts with atomically defined junctions for improved photocatalytic activities†

Min Zhang, Muhammad Arif, Yuxiang Hua, Bo Qiu, Yue Mao and Xiaoheng Liu *

The use of semiconductor photocatalysts to generate electrons with efficient reducing capability for organic photoreduction synthesis and the removal of harmful substances has become a hotspot in the field of green chemistry research. In this work, α-MnO_2 nanocubes and α-MnO_2@$MnIn_2S_4$ hybrid photocatalysts with a core–shell structure were synthesized successively by a two-step method. XRD and XPS verified the coexistence of the two substances (α-MnO_2 and $MnIn_2S_4$) in hybrid systems. According to the SEM and TEM characterization, it is clearly seen that $MnIn_2S_4$ nanosheets grow on α-MnO_2 nanocubes to form a hierarchical structure. Furthermore, HRTEM showed that the interface contact between α-MnO_2 and $MnIn_2S_4$ resulted in an atomically defined junction. The photocatalytic performance of the composite catalyst was evaluated by reducing 4-nitroaniline to 4-phenylenediamine and Cr(VI) to Cr(III), respectively. The results show that the catalytic activity of the composite material is effectively improved compared to that of the single components. The Z-scheme electron transport mechanism was proved by ultraviolet-visible diffuse reflectance spectroscopy, valence band XPS, energy band structure calculation and active species detection experiments. The constructed Z-scheme hierarchical α-MnO_2@$MnIn_2S_4$ system with an atomically defined junction can improve the redox performance of semiconductors for organic synthesis and environmental remediation.

Received 11th October 2020
Accepted 3rd December 2020

DOI: 10.1039/d0na00848f

rsc.li/nanoscale-advances

1 Introduction

Recently, with the development of industrialization, human society's demand for industrial chemicals has been increasing, and the issue of environmental pollution has also been paid more and more attention to.[1–3] 4-Phenylenediamine (4-PDA) is a widely used industrial chemical raw material. It can be used in the preparation of azo dyes, as well as in the preparation of developers, rubber antioxidants, and copper–iron indicators.[4–8] The industrial preparation of 4-PDA is mainly carried out by using 4-nitroaniline (4-NA) as a raw material and adopting industrial hydrogenation.[9,10] This method is restricted by strict reaction conditions and complicated procedures. In recent years, some research studies involving photocatalytic and electrocatalytic methods to prepare 4-PDA have attracted more and more attention.[11,12] Among these methods, highly selective photoreduction of 4-NA to 4-PDA in water systems has become a powerful technology. Moreover, dealing with highly toxic hexavalent chromium is a difficult task in the treatment of world environmental pollution.[13,14] Based on trivalent chromium's low toxicity and easy flocculation into $Cr(OH)_3$ in an alkaline environment, reducing Cr(VI) to trivalent chromium has become a key procedure for environmental remediation.[15,16] Among the currently developed reduction methods, photocatalytic reduction has shown potential application prospects compared with high-cost chemical reduction methods[17] and biological reduction methods[18] with high environmental requirements. Therefore, visible-light-driven semiconductor photocatalysis has received extensive attention in these fields because of its low cost, environmental friendliness and unique reaction mechanisms and easy availability of materials.[19–22] Importantly, photogenerated electrons generated by semiconductors with a deeper conduction band top have extremely strong reducibility and have attracted the attention of researchers.

Manganese-based materials (MnO_2, Mn_3O_4, $MnFeO_4$, $MnSiO_3$, and metal–Mn LDH) are widely used in photocatalytic environmental remediation, supercapacitors, lithium–sulfur batteries, and guided cancer treatments due to their low-cost, easy availability, environmental friendliness, high theoretical capacitance, and narrow band gap.[23–27] The visible light absorption capability of manganese oxide among them is high due to its narrow band gap which makes it a promising candidate for photocatalysis. Gaigneaux *et al.* reported a plasma chemical reduction method to prepare three kinds of α-, γ- and δ-MnO_2. Tartrazin yellow was selected as the model pollutant

Key Laboratory of Education Ministry for Soft Chemistry and Functional Materials, Nanjing University of Science and Technology, Nanjing 210094, Jiangsu Province, China. E-mail: xhliu@njust.edu.cn

† Electronic supplementary information (ESI) available. See DOI: 10.1039/d0na00848f

for photocatalytic activity evaluation, and the results showed that α-MnO_2 has achieved the best overall photocatalytic performance.[28] On the other hand, the weaker photoreduction ability caused by the higher conduction band potential and the high recombination efficiency of photogenerated carriers caused by the narrow band gap limit the in-depth application of MnO_2 in the photocatalytic industry. Fortunately, the preparation of composite nanomaterials and the introduction of the concept of heterojunction catalysis greatly improve this defect. Leung *et al.*[29] *in situ* synthesized a TiO_2/MnO_2 heterojunction catalyst by a hydrothermal method and used the catalyst for vacuum ultraviolet (VUV) photocatalytic oxidation of toluene degradation. The good contact of the heterojunction structure of TiO_2/MnO_2 effectively inhibited the recombination of photoexcited electron–hole pairs and improved the catalytic activity. Qiu *et al.*[30] built a Z-scheme mesoporous α-MnO_2/Mn_3O_4 heterojunction to promote its photocatalytic oxidation activity by using the characteristics of Mn having multivalent states. It is proposed that the heterojunction of multivalent manganese oxide can efficiently prevent the recombination of photogenerated carriers.

Furthermore, $MnIn_2S_4$, which belongs to the AB_2X_4 (A = Cu, Cd, and Mn; B = Al, Ga, and In; X = S, Se, and Te) family,[31–33] has also received considerable attention in the field of photocatalysis due to its suitable band gap and simple preparation. Chen *et al.*[34] synthesized a direct Z-scheme 2D/2D $MnIn_2S_4$/g-C_3N_4 structure, which has high photocatalytic activity for the treatment of pharmaceutical wastewater and hydrogen evolution.

In this work, α-MnO_2 nanocubes were obtained through the guiding effect of surfactant and annealing treatment, and then a multi-stage α-MnO_2@$MnIn_2S_4$ composite photocatalyst was synthesized *in situ* by a solvothermal reaction after adsorption of Mn^{2+} and In^{2+}. SEM and TEM showed that the synthesized catalyst was $MnIn_2S_4$ nanosheets coated on α-MnO_2 nanocubes making an α-MnO_2@$MnIn_2S_4$ core–shell structure. Compared with the single materials, the composite catalyst exhibits excellent catalytic activity and structural stability in reducing 4-NA and Cr(VI).

2 Experimental

2.1 Materials

All reagents were used without any further purification in this research. Manganese sulfate monohydrate ($MnSO_4 \cdot H_2O$, AR), cyclohexane (C_6H_{12}), manganese chloride tetrahydrate ($MnCl_2 \cdot 4H_2O$, AR), indium chloride ($InCl_3 \cdot 4H_2O$, AR) and ammonium formate (CH_5NO_2) were bought from Aladdin Industrial Corporation. Potassium dichromate (KCr_2O_7), potassium permanganate ($KMnO_4$), cetyltrimethylammonium bromide (CTAB), ammonium bicarbonate (NH_4HCO_3), and thioacetamide (TAA) were purchased from Sinopharm Group Chemical Reagent Co., Ltd.

2.2 Catalyst synthesis

2.2.1 Preparation of α-MnO_2 nanocubes. The α-MnO_2 nanocubes were prepared by calcining the δ-MnO_2 precursor, where the δ-MnO_2 precursor comes from the etching of $MnCO_3$ nanocubes using $KMnO_4$. Typically,[30,35] 4 g of CTAB was added to 100 mL of cyclohexane, and then 5 mL of *n*-butanol and 0.8 M NH_4HCO_3 were added. After stirring until the solution became clear, 5 mL of 0.4 M $MnSO_4$ solution was added dropwise. The conversion of the solution from a clear to a milky white suspension indicated the formation of $MnCO_3$ nanocubes. After centrifugal drying and washing with water and ethanol, 1 g of $MnCO_3$ was dispersed in a certain amount of 0.032 M $KMnO_4$ solution with continuous magnetic stirring. The reaction process is as follow (1):

$$2MnO_4^- + MnCO_3 + H_2O \rightarrow 2MnO_4^{2-} + MnO_2 + 2H^+ + CO_2 \quad (1)$$

After filtering and separation of the above suspension, it was dried at 60 °C for 8 hours to obtain a δ-MnO_2 precursor. Furthermore, the obtained δ-MnO_2 precursor was heat-treated in an air atmosphere at 500 °C for 2 h at a heating rate of 5 °C min^{-1} to obtain α-MnO_2 nanocubes.

2.2.2 Preparation of α-MnO_2@$MnIn_2S_4$. The α-MnO_2@-$MnIn_2S_4$ composite photocatalyst was prepared by a solvothermal method. A certain amount of α-MnO_2 was added to 60 mL of ethylene glycol and sonicated for 60 min. Immediately, 1 mmol $MnCl_2$, 2 mmol $InCl_3$, and 4 mmol TAA were added to the above suspension in sequence and kept under stirring for 1 h. The reaction precursor solution was transferred into a Teflon-lined stainless steel autoclave with a capacity of 100 mL, which was heated and maintained at 180 °C for 24 h. The α-MnO_2@$MnIn_2S_4$ composite photocatalyst was obtained by natural cooling to room temperature, washing with deionized water and ethanol, centrifugation, and drying at 60 °C overnight. According to the added amount of α-MnO_2 (0.25 mmol, 0.5 mmol, 0.75 mmol, and 1 mmol, respectively), the as-prepared photocatalysts were named M–MIS-*x* (*x* = 1, 2, 3, and 4). For comparison, the pure $MnIn_2S_4$ (MIS) sample can be synthesized without adding any α-MnO_2 nanocubes by the same fabrication methods.

2.3 Characterization of the catalyst

The morphology of the fabricated samples was demonstrated by using an electron microscope (SEM and TEM, JEM-2100). X-ray diffraction (XRD, D8 Advance X-ray diffractometer, Cu K, λ = 1.5406 Å, tube voltage 40 kV, tube current 40 mA) was used to characterize the crystallinity and structure of the catalyst. The surface element composition and valence state of the sample were determined by X-ray photoelectron spectroscopy. The ultraviolet-visible diffuse reflection spectrum (DRS) was used to show the light absorption capacity of the catalyst using BaSO4 as the substrate.

2.4 Evaluation of photocatalytic performance

The photocatalytic activity of the catalyst was evaluated by reducing 4-nitroaniline (4-NA) and Cr(VI). In a typical catalytic process, 50 mg of the sample was dispersed in 50 mL 4-NA (10 mg L^{-1}) ultrasonically, and ammonium formate (150 mg) was added as a hole trapping agent. Before the irradiation, the

adsorption–desorption equilibrium was achieved in the dark and in a nitrogen environment for 1 h. At regular intervals, 3 mL of the photocatalytic reaction solution was taken out. The catalyst in the solution was removed with centrifugation and a 0.22 μm drainage filtration membrane. The product detection by using a UV-Vis spectrophotometer shows the characteristic absorption peak of 4-NA at 381.7 nm, while 293.7 nm and 238.1 nm belong to the characteristic absorption peaks of 4-phenylenediamine (4-PDA). In addition, for the photocatalytic reduction of Cr(VI), 50 mg of the sample was dispersed in 50 mL of 50 mg L^{-1} Cr(VI) solution and adsorbed in a dark room for 1 h. Under visible light irradiation, 1 mL of the solution was taken at regular intervals of 20 min and centrifuged to remove the catalyst. The concentration of Cr(VI) was detected at 540 nm by the normal diphenylcarbazide (DPC) method.

2.5 Electrochemical performance test

The transient photocurrent and electrochemical impedance spectra (EIS) were obtained on a CHI 760E electrochemical workstation. The standard three-electrode system was composed of the photocatalyst (0.2 mg sample loaded on a 1.0 cm^2 conductive glass area), a platinum wire, and a saturated Ag/AgCl electrode, which were used as the working electrode, counter electrode, and reference electrode in the test system. The transient photocurrent test of the sample was carried out in 0.5 M Na_2SO_4 aqueous solution with a 300 W xenon lamp with a 420 nm cutoff filter. The electrochemical impedance spectroscopy test of the sample was carried out in 0.1 M KCl solution containing 2.5 mM $K_3[Fe(CN)_6]/K_4[Fe(CN)_6]$ as the electrolyte.

3 Results and discussion

In this work, we constructed a heterojunction photocatalyst by growing $MnIn_2S_4$ nanosheets *in situ* on the surface of α-MnO_2 nanocubes to efficiently reduce 4-NA and Cr(VI), constructing a core–shell-like α-MnO_2@$MnIn_2S_4$ hierarchical heterostructure as illustrated schematically in Fig. 1. Firstly, $MnCO_3$ nanocubes were synthesized by room temperature solvent orientation. After an oxidation–reduction reaction with $KMnO_4$ and annealing treatment, the α-MnO_2 nanocubes are obtained. Finally, $MnIn_2S_4$ nanosheets were grown *in situ* on the surface of α-MnO_2 nanocubes by a solvothermal reaction. It should be noted that Mn^{2+} will be preferentially adsorbed to the α-MnO_2 surface due to the negative charge of the α-MnO_2 surface[36] and the Fajans rules during the stirring process before the solvothermal reaction,[37] which is beneficial in the *in situ* growth of $MnIn_2S_4$. The photocatalytic functions of α-MnO_2 and $MnIn_2S_4$ are concentrated in a hierarchical core–shell structure, which facilitates the separation and migration of photogenerated electrons and holes, and provides a large number of active sites for the reduction reaction.

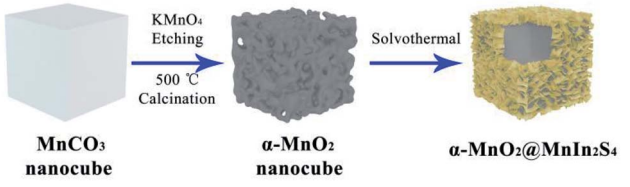

Fig. 1 Schematic illustration of the synthetic process of hierarchical α-MnO_2@$MnIn_2S_4$.

3.1 Structure and morphology

The powder X-ray diffraction (XRD) technology was used to investigate the crystal structure and phase purity of pure $MnIn_2S_4$ nanosheets, α-MnO_2 nanocubes, and all M–MIS nanocomposites with different α-MnO_2 contents. Fig. S1† displays the XRD pattern of the as-prepared $MnCO_3$ precursor in which all the characteristic crystal peaks are consistent with the cubic phase (JCPDS no: 44-1472).[38] As shown in Fig. S2,† the pure MnO_2 sample shows diffraction peaks at 12.8°, 18.1°, 28.8°, 36.7°, 37.5°, and 49.9°, which can be assigned to the (110), (200), (310), (400), (211) and (411) crystallographic planes of cubic α-MnO_2 (JCPDS no: 44-0141).[39] Along with the coupling of $MnIn_2S_4$ nanosheets and α-MnO_2 to form the α-MnO_2@-$MnIn_2S_4$ nanocomposite catalyst, the M–MIS-*x* series samples show diffraction peaks at 14.3°, 27.6°, 33.4°, and 48°, respectively, which correspond to the (111), (311), (400) and (440) crystal planes of cubic phase (JCPDS no: 65-7474) $MnIn_2S_4$.[34] It is worth noting that there is no impurity diffraction characteristic peak of In_2S_3 or MnS in the pure $MnIn_2S_4$ and M–MIS-*x* composite catalysts. The hierarchical composite catalyst assembled using α-MnO_2 and $MnIn_2S_4$ is beneficial to the carrier transport between the interfaces and improves the photocatalytic activity.[40,41]

The morphology of the as-prepared materials was characterized by SEM and TEM. Fig. 2a–c shows the morphology of $MnCO_3$ as the precursor of α-MnO_2. The size of the cube with a smooth surface is about 200 nm. As shown in Fig. S3,† after the reaction of $MnCO_3$ with $KMnO_4$, the morphology of the nanocube is still maintained, and "small thorns" of nanosheets are grown on the smooth surface. After the annealing treatment, the surface of the δ-MnO_2 nanocube becomes rough due to the etching of the ions and voids are generated inside, which will facilitate the adsorption of Mn^{2+} and In^{3+} to form a heterojunction *in situ* (Fig. 2d–f). The HRTEM image of a single nanocube (Fig. 2i-II) exhibits the lattice lines with a spacing of about 0.692 nm and 0.245 nm, which are in good agreement with the (110) and (400) crystal plane distances of α-MnO_2,[42,43] respectively, and the angle between the two crystal planes is 45°. $MnIn_2S_4$ was crystallized in three-dimensional nanoflakes as shown in Fig. 2g and h, and this two-dimensional structure can provide more catalytic sites. Similarly, the lattice fringes attributed to the (222) and (400) crystal planes of $MnIn_2S_4$ are 0.309 nm and 0.268 nm, respectively (Fig. 2i-I).[34] Next, the thin $MnIn_2S_4$ nanosheets were grown on the surface of the α-MnO_2 cubes by a solvothermal method. After the reaction, $MnIn_2S_4$ nanosheets uniformly covered the surface of the α-MnO_2 cube and had a good overall 3D morphology (Fig. 2j). The layered cubic core–shell structure of α-MnO_2@$MnIn_2S_4$ is shown by the TEM images (Fig. 2k). No visible interlayer gaps were found between the $MnIn_2S_4$ shell and the α-MnO_2 core (Fig. S4†),

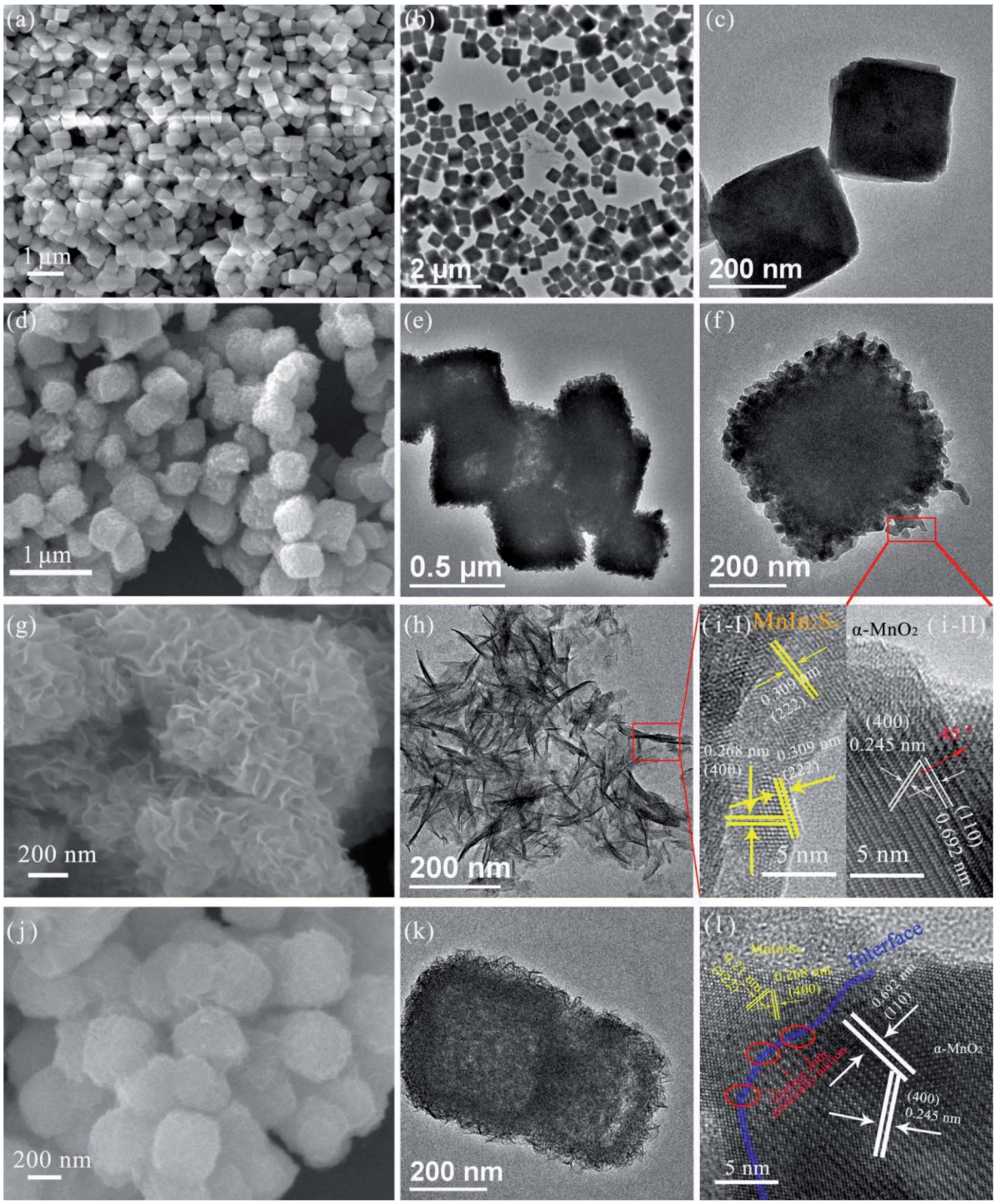

Fig. 2 SEM and TEM images of (a–c) $MnCO_3$ nanocubes, (d–f) α-MnO_2 nanocubes, (g and h) $MnIn_2S_4$ nanosheets, and (j and k) M–MIS-2, and HRTEM images of (i) α-MnO_2 (II) and $MnIn_2S_4$ (I) and (l) M–MIS-2.

indicating close contact between the two components. The HR-TEM image shows the heterojunction between layered $MnIn_2S_4$ and α-MnO_2 (Fig. 2l), in which lattice fringes can be assigned to cubic α-MnO_2 and hexagonal $MnIn_2S_4$ crystal planes can be seen. In particular, the red elliptical area in Fig. 2l clearly shows the interface with an atomic junction between the crystal planes of the two materials. These results provide clear evidence of the formation of an α-MnO_2@$MnIn_2S_4$ core–shell structure.

Besides, the SEM elemental mapping of M–MIS-2 is shown in Fig. 3a. It can be seen from the images that Mn, O, In, and S elements all appear on the hierarchical nanocubes, which verifies the successful recombination of $MnIn_2S_4$ and α-MnO_2 from the side. In order to clearly understand the combination of

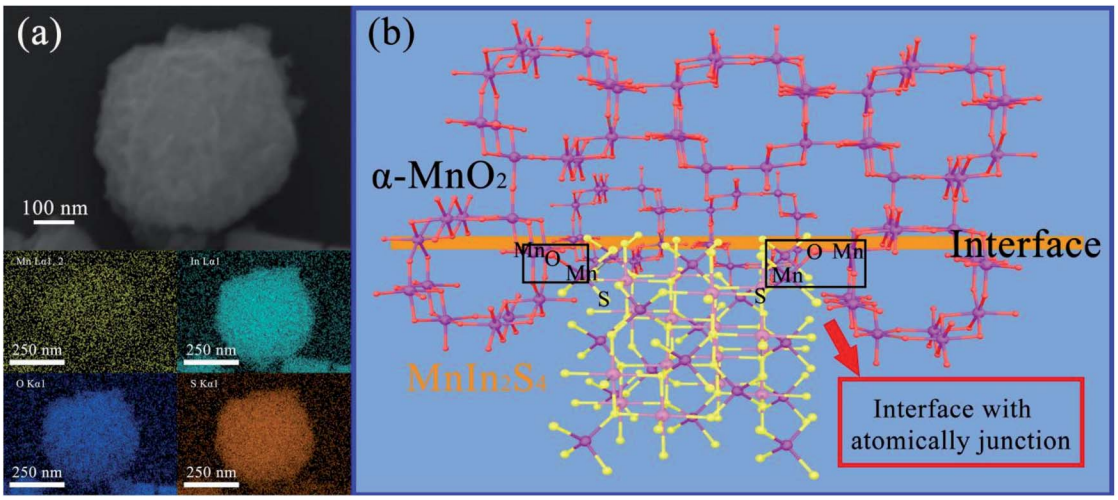

Fig. 3 (a) SEM elemental mapping of M–MIS-2 and (b) schematic illustration of the interface between α-MnO_2 and $MnIn_2S_4$.

the two components at the interface, a schematic illustration of the interface and atomic-junction combination of α-MnO_2 and $MnIn_2S_4$ is shown based on HR-TEM and SEM elemental mapping (Fig. 3b). The negative charge oxygen atoms in α-MnO_2 crystals are exposed on the surface.[44,45] Mn^{2+} and In^{3+} exist in the suspension system at the same time, and Mn^{2+} will be preferentially anchored on the surface of α-MnO_2 according to the Fajans rules.[37] These atomically-defined-junction and close interface contact facilitate the transport and separation of photo-generated electrons and improve the catalytic activity of the photocatalyst.

3.2 Surface element analysis

The surface elements and valence states of the as-prepared photocatalyst were characterized by XPS. Herein, the interaction mechanism between α-MnO_2 and $MnIn_2S_4$ can be further confirmed by Mn $2p_{3/2}$, $2p_{1/2}$, and S 2p XPS analysis.[46] Fig. S5† shows the full-scale XPS spectra for α-MnO_2@$MnIn_2S_4$ (M–MIS-2) and single α-MnO_2 and $MnIn_2S_4$. Among them, the M–MIS-2 XPS spectrum contains Mn, In, O, and S elements, which confirms the coexistence of α-MnO_2 and $MnIn_2S_4$ in the composite materials. This result is completely consistent with SEM elemental mapping (Fig. 3a). The Mn 2p spectra of M–MIS-2 are displayed in Fig. 4a and show the characteristic peaks assigned to Mn^{2+} (641.48 eV and 652.32 eV) and Mn^{4+} (643.92 eV and 653.71 eV).[47,48] Compared with composite materials, the position of the characteristic peak of Mn $2p_{3/2}$ and Mn $2p_{1/2}$ in single α-MnO_2 and $MnIn_2S_4$ is shifted, which is closely related to the heterojunction formation by the two materials.[49] It can be seen from Fig. 4b that the O 1s high-resolution spectra of α-MnO_2 and M–MIS-2 samples show the characteristic peak at 529.43 eV, which belongs to Mn–O–Mn.[50] Moreover, the characteristic peaks located at 531.37 eV and 530.31 eV in α-MnO_2 and M–MIS-2 can be assigned to Mn–O–H, respectively.[51] The Mn–O–H shift to low binding energy is because the chemical state of Mn on the surface of α-MnO_2 is 4+, which is higher than that (2+) of Mn in the $MnIn_2S_4$ on the surface of M–MIS-2. As shown in Fig. 4c, the binding energy of S 2p in $MnIn_2S_4$ was detected at 161.30 eV and 162.37 eV, respectively. Correspondingly, the characteristic peak of the composite catalyst (M–MIS-2) has a slight shift towards high binding energy (161.25 eV and 162.25 eV, respectively).[52] The In 3d spectra of $MnIn_2S_4$ and M–MIS-2 are illustrated in Fig. 4d. The binding energies of the doublets are $3d_{5/2}$ (444.88 eV and 444.77 eV) and $3d_{3/2}$ (452.50 eV and 452.37 eV), respectively. As mentioned earlier, the shift in binding energy of the heterojunction sample indicates a strong interaction between $MnIn_2S_4$ nanosheets and α-MnO_2 nanocubes, which enhances the migration efficiency of photogenerated carriers, thereby improving the catalytic activity of the catalyst.

3.3 Optical properties, band structure and carrier separation efficiency

Many factors affect the activity of photocatalysts, such as the band gap, crystal structure, crystal plane orientation and optical properties.[53,54] Among them, optical properties are the most important characteristics that determine the application of photocatalytic materials in the field of photocatalysis. Fig. 5a shows the UV-Vis diffuse reflectance spectra of M–MIS with different molar ratios and single materials. Compared with other materials, α-MnO_2 has higher band-edge absorption in the visible and near-infrared regions, indicating that it is a narrow band gap semiconductor. The absorption band edge of $MnIn_2S_4$ is about 560 nm. With the increase of the content of α-MnO_2 in the α-MnO_2@-$MnIn_2S_4$ heterostructure, the absorption of the composite materials in visible light gradually increases, which is beneficial for the easy excitation of the semiconductor under visible-light and generates more carriers. Furthermore, the band gap width of α-MnO_2 and $MnIn_2S_4$ calculated using the Kubelka–Munk formula is determined to be 1.53 eV and 2.23 eV, respectively, which are consistent with those in the reported literature.[30,34] Similarly, the positions of the bottom of the valence band (VB) of α-MnO_2 and $MnIn_2S_4$ are determined from the VB-XPS analysis and it was found to be 2.61 eV and 1.42 eV, respectively (Fig. 5c). Furthermore, the CB potential of α-MnO_2 and $MnIn_2S_4$ at the point of zero charges was theoretically calculated from eqn (2):[55]

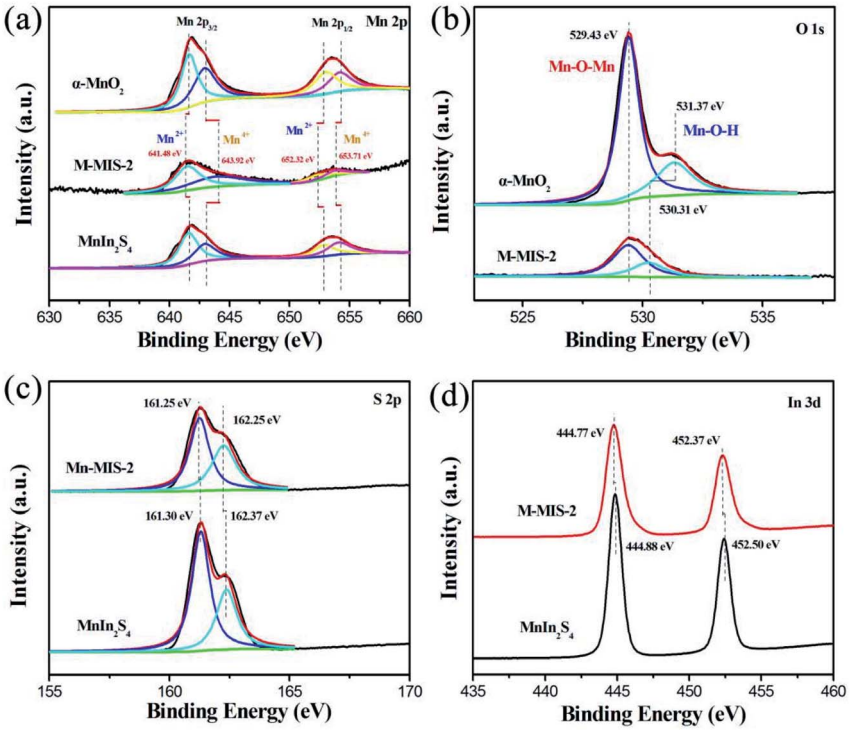

Fig. 4 High-resolution (a) Mn 2p, (b) O 1s, (c) S 2p and (d) In 3d XPS spectrum for the α-MnO_2@$MnIn_2S_4$ (M–MIS-2), and pure α-MnO_2, and $MnIn_2S_4$.

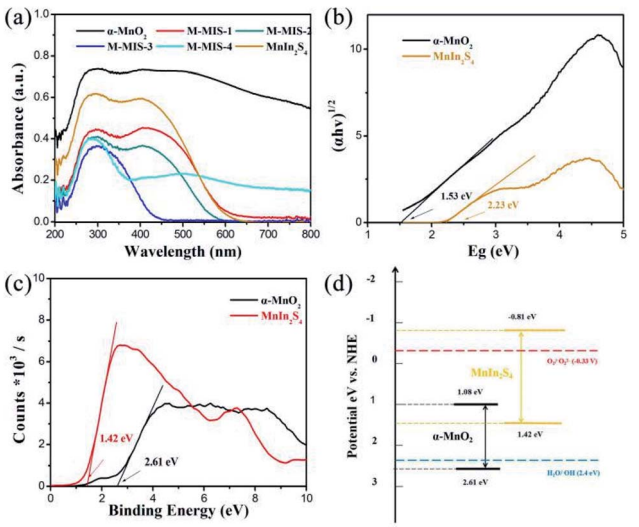

Fig. 5 (a) UV-vis diffuse reflectance spectra of different samples, (b) calculated band gap patterns based on UV-vis diffuse reflectance spectra of α-MnO_2 and $MnIn_2S_4$, (c) XPS valence band spectrum and (d) energy band structure of α-MnO_2 and $MnIn_2S_4$.

$$E_g = |E_{CB} - E_{VB}| \quad (2)$$

where E_g is the band gap energy. The calculated E_{CB} values of α-MnO_2 and $MnIn_2S_4$ are 1.08 eV and −0.81 eV, respectively (Fig. 5d).

Moreover, the migration rate of photogenerated carriers is also an important factor of the photocatalytic activity of the catalyst. To further compare the migration and separation efficiency of photogenerated electrons–holes of the different materials, the transient photocurrent responses were measured during several on–off intermittent irradiation cycles.[56] As shown in Fig. 6a, the M–MIS-2 exhibited a much higher photocurrent response than other single photocatalysts (α-MnO_2 and $MnIn_2S_4$), indicating that the composite material has a higher charge generation and transfer efficiency. This carrier migration in the composite catalyst leads to an effective e_{CB}^-–h_{VB}^+ separation and a lower recombination rate in the M–MIS-2 sample, ultimately leading to enhanced photocatalytic performance.[57] Furthermore, EIS measurements are used to gain a deeper understanding of the photogenerated charge carrier transfer process and recombination behavior. Fig. 6b displays a typical Nyquist plot of different samples under dark conditions. It can be seen that the α-MnO_2 electrode forms a partial

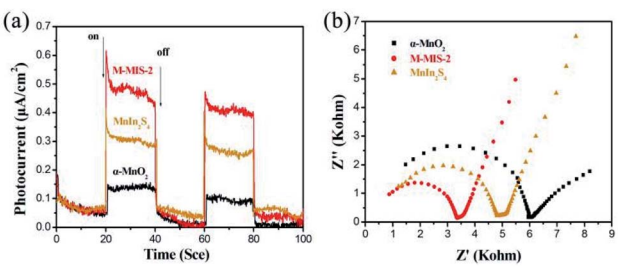

Fig. 6 (a) Photocurrent density and (b) EIS Nyquist plots of α-MnO_2, $MnIn_2S_4$ and M–MIS-2.

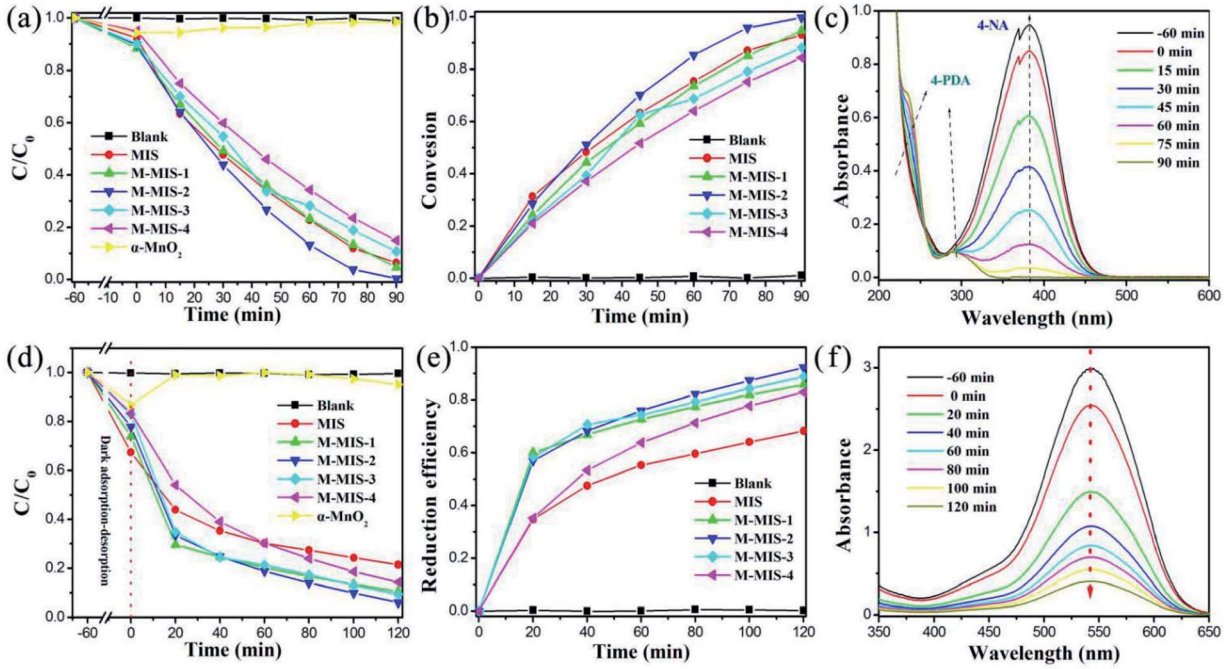

Fig. 7 (a and d) Time-course variation of the 4-NA and Cr(VI) solution under visible light irradiation with photocatalysts, (b) the conversion of selective photo-reduction from 4-NA to 4-PDA in the presence of different catalysts, (c) UV-vis absorption spectra of 4-NA at different irradiation times using M–MIS-2 with the addition of ammonium formate and N_2, (e) Cr(VI) reduction efficiency of 50 mg of different catalysts under visible light for 120 min with different initial Cr(VI) concentrations, and (f) UV-vis absorption spectra of aqueous Cr(VI) (50 mg L^{-1}) treated with M–MIS-2.

semicircle with a diameter larger than that of the other samples. The semicircle in the high-frequency region reflects the charge transfer resistance and constant phase elements at the photocatalyst/electrolyte interface. The radius of the semicircle of M–MIS-2 is the smallest at any frequency, indicating that the charge transfer resistance is smaller, which leads to a better electronic conductivity and charge separation efficiency.[58] Furthermore, the high electron–hole separation efficiency in the M–MIS composite photocatalyst was analyzed by steady-state photoluminescence (PL) spectroscopy. As can be seen from Fig. S6,† M–MIS-2 exhibits a lower PL emission intensity compared to α-MnO_2 and $MnIn_2S_4$, which means that there is a faster charge transfer rate at the contact interface of the composite catalyst, and it has a better separation efficiency than a single component.

3.4 Photocatalytic performance

The photocatalytic performance of the synthesized α-MnO_2@-$MnIn_2S_4$ heterojunctions was characterized by the photoreduction from 4-NA to 4-PDA with a visible light source ($\lambda > 420$ nm). Obviously, pure α-MnO_2 has no activity towards 4-PDA evolution from 4-NA, and the dark adsorption on the surface of α-MnO_2 gradually desorbs 4-NA molecules during the light process. Different amounts of α-MnO_2 were compounded with $MnIn_2S_4$, and the photocatalytic performance of M–MIS on 4-NA was greatly improved (Fig. 7a). In particular, M–MIS-2 has the best reduction efficiency, with a conversion efficiency of 99.6% for photoreduction of 4-NA to 4-PDA within 90 min (Fig. 7b). As shown in Fig. 7c, with the gradual decrease in the intensity of the main absorption peak of 4-nitroaniline at 381.7 nm, at the same time the characteristic absorption peak intensities of 4-phenylenediamine at 293.7 nm and 238.1 nm consecutively increase. As shown in Fig. S7†, the color of the reaction solution gradually changed from light yellow to colorless after 90 minutes of visible light irradiation, indicating the highly selective conversion efficiency of 4-NA to 4-PDA.

Similarly, the M–MIS heterojunction catalyst also shows higher photocatalytic efficiency towards the photoreduction of Cr(VI). As shown in Fig. 7d, when single α-MnO_2 is used as a catalyst, the content of Cr(VI) changes little, which is attributed to the adsorption effect of the high specific surface area of the mesoporous α-MnO_2. The composite catalysts showed higher catalytic activity than pure MIS in reducing Cr(VI). M–MIS-2 showed the best photocatalytic reduction efficiency among all the catalysts, reaching 94% (Fig. 7e and f). Therefore, the above results indicate that the M–MIS-2 sample exhibits excellent visible-light-driven photocatalytic reduction performance, indicating that the α-MnO_2@$MnIn_2S_4$ heterojunction is an attractive material for environmental remediation and organic conversion.

Besides the photocatalytic activity of the target material, its catalytic stability is also an important factor in measuring the application prospects of the catalyst. It can be seen in Fig. 8a that the photoreduction reactions of 4-NA over M–MIS-2 can still maintain the conversion rate above 92%. The slight decrease may be due to the loss of the catalyst. The sample after four reduction experiments was characterized by XRD (Fig. 8b), and the results show that its crystal shape did not change

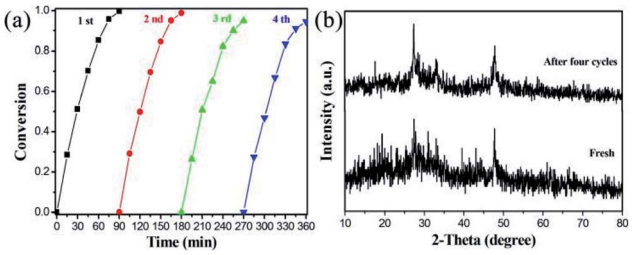

Fig. 8 (a) Cycles of photocatalytic reduction of 4-NA by M–MIS-2; (b) XRD patterns of M–MIS-2 after four cycle experiments.

significantly and had good stability. In addition, the SEM images of the M–MIS-2 catalyst before and after the reaction are shown in Fig. S8.† The morphology of the sample before and after the reaction is still maintained.

3.5 Possible photocatalytic mechanism

As we all know, the active species (such as superoxide radicals ($^{\bullet}O_2^-$), holes (h^+) and hydroxyl radicals ($^{\bullet}OH$)) in the photocatalytic reaction system play an important role. In order to detect these species, we use $AgNO_3$, isopropanol (IPA), and disodium ethylenediaminetetraacetic acid (EDTA–2Na) with a concentration of 1 mM as the e^-, $^{\bullet}OH$ and h^+ capture agents.[14,59,60] Obviously, it can be observed from Fig. 9 that with the addition of $AgNO_3$, the reduction efficiency of the catalyst towards Cr(VI) significantly decreases, indicating that e^- is an important active species participating in the reduction reaction. After IPA was introduced into the photoreduction system, the catalytic efficiency decreased slightly, which may be because some of the $^{\bullet}OH$ was produced by e^- and competed with the Cr(VI) reduction process. When the EDTA–2Na is added, it can be found that the catalytic reduction efficiency was significantly improved, which is due to the addition of the hole trapping agent and it inhibits the recombination of photogenerated electrons–holes, consequently, improving the rate and utilization of electron migration to the catalyst surface. After adding BQ in the system, the photocatalytic reduction efficiency also decreased, which is due to the generation of $^{\bullet}O_2^-$ from photogenerated electrons. When the $^{\bullet}O_2^-$ was captured, the balance of the reaction ($e^- + O_2 \rightarrow {}^{\bullet}O_2^-$) moves to the right, reducing the photogenerated electrons in the reaction system. Therefore, during the photocatalytic Cr(VI) reduction, the electrons are the main participating species.

To further demonstrate the photocatalytic reaction mechanism of α-MnO_2@$MnIn_2S_4$, the detection of superoxide radicals ($^{\bullet}O_2^-$) and hydroxyl radicals ($^{\bullet}OH$) can be carried out. The enhanced photocatalytic ability was confirmed by conversion experiments of nitro blue tetrazolium (NBT) and terephthalic acid (TA). Due to the exclusive reaction between $^{\bullet}O_2^-$ and NBT, NBT can be used to detect the presence of $^{\bullet}O_2^-$ in the photoreaction.[61] Therefore, in the photocatalytic reaction, a low NBT concentration means that a large amount of $^{\bullet}O_2^-$ is produced in the system. It can be seen from Fig. 10a that, as the photocatalytic reaction time increases, the NBT concentration continues to decrease, confirming that the α-MnO_2@$MnIn_2S_4$ (represented by M–MIS-2) system can produce $^{\bullet}O_2^-$ during the photoreaction. The NBT measurement of all samples after 60 min is shown in Fig. 11b. Taking into account the effect of error, no change in the concentration of NBT was observed in the single α-MnO_2 system, indicating that $^{\bullet}O_2^-$ was not produced during the photoreaction. In addition, M–MIS-2 produced the highest level of $^{\bullet}O_2^-$. The $^{\bullet}O_2^-$ is produced by the reaction of O_2 with photogenerated electrons and more O_2 indicates high separation efficiency of photogenerated carriers in the α-MnO_2@$MnIn_2S_4$ system.

At the same time, high $^{\bullet}O_2^-$ production concentration are accompanied by high $^{\bullet}OH$ concentrations.[62] The $^{\bullet}OH$ can be

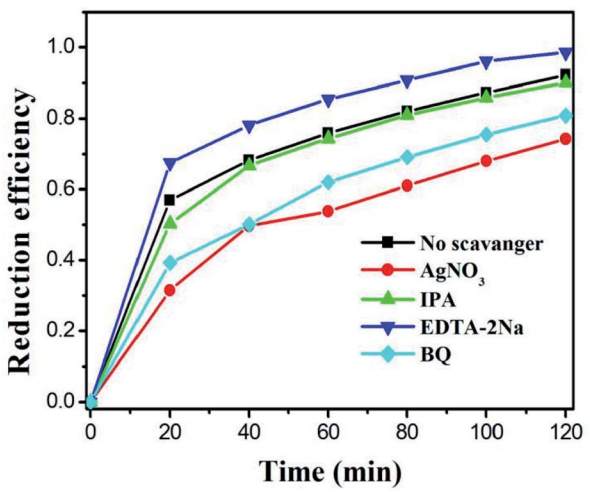

Fig. 9 Effects of different scavengers on Cr(VI) reduction in the presence of M–MIS-2.

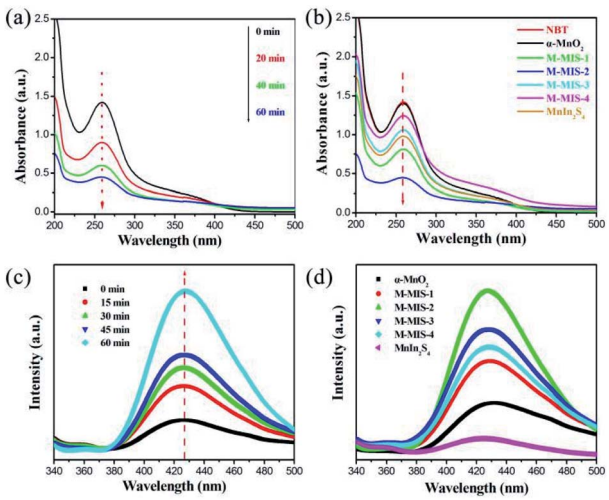

Fig. 10 Temporal UV-vis absorption spectral changes of NBT over (a) M–MIS-2 with different times and (b) all different photocatalysts (300 W Xe lamp, illumination time = 60 min, NBT dosage = 0.025 mM); PL spectral variations in 2 mM NaOH solution with the addition of 0.5 mM terephthalic acid using a (c) M–MIS-2 Z-scheme photocatalyst at different times and (d) single α-MnO_2, $MnIn_2S_4$ and M–MIS-x (x = 1, 2, 3, 4).

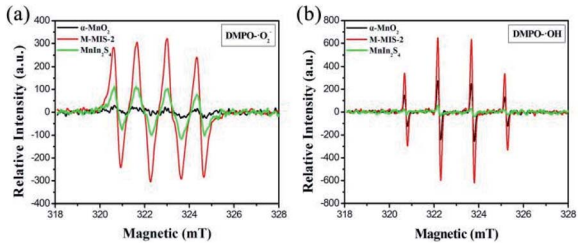

Fig. 11 ESR spectra of radical adducts trapped by DMPO: (a) DMPO–$^{\cdot}O_2^-$ and (b) DMPO–$^{\cdot}$OH in the α-MnO_2, $MnIn_2S_4$ and M–MIS-2 dispersion solution.

equally divided with terephthalic acid (TA) to form 2-hydroxyterephthalic acid (TAOH), which exhibits a characteristic peak at 425 nm when excited at a wavelength of 325 nm, so TA can be applied to detect $^{\cdot}$OH. As shown in Fig. 10c, the gradual increase of the fluorescence intensity over time indicates that $^{\cdot}$OH is gradually generated during the illumination process. In addition, the fluorescence signal of M–MIS-*x* is stronger than that of single α-MnO_2 and $MnIn_2S_4$ after 60 min of irradiation (Fig. 10d). The M–MIS-2 has the highest signal intensity, which further proves that the composite material can produce higher active oxygen performance. This is consistent with the NBT detection result, which indicates that the composite catalyst improves the separation efficiency of carriers and produces more active components.

Furthermore, as shown in Fig. 11a, the ESR signal for DMPO–$^{\cdot}O_2^-$ can be observed for $MnIn_2S_4$ and M–MIS-2, which means that $^{\cdot}O_2^-$ was generated in the reaction system during visible light irradiation. Moreover, the characteristic peak of DMPO–$^{\cdot}$OH for pure $MnIn_2S_4$ does not appear under visible light irradiation (Fig. 11b) but four weak peaks were detected for pure α-MnO_2. As for M–MIS-2 heterojunction composites, the DMPO–$^{\cdot}$OH signal intensities of $^{\cdot}$OH are obviously much higher than those in pure α-MnO_2, which can be attributed to the construction of the atomically defined heterojunction to improve $^{\cdot}$OH production.

Based on the above test results and experimental phenomenon, a possible Z-scheme photocatalytic reduction mechanism of 4-NA and Cr(VI) using α-MnO_2@$MnIn_2S_4$ is proposed. As illustrated in Fig. 12, under visible light irradiation, the electrons located on the valence band (VB) of α-MnO_2 and $MnIn_2S_4$ are excited and then transfer to the conduction band (CB), while holes remain on the VB. At the interface of α-MnO_2 and $MnIn_2S_4$, electrons in the CB of α-MnO_2 are transferred along the interface to the VB of $MnIn_2S_4$ to recombine with holes. The electrons remaining in the CB of $MnIn_2S_4$ gain relatively more negative potential energy and have stronger reducibility, and then react with 4-NA and Cr(VI), hence reducing them to 4-PDA and Cr(III). In contrast to the traditional type-II electron transport mechanism (Fig. S9†), the e^- in the CB of $MnIn_2S_4$ migrates to the CB of α-MnO_2 and the h^+ of α-MnO_2 is transferred to the VB of $MnIn_2S_4$. Since the CB potential of α-MnO_2 is more positive than that of $O_2/^{\cdot}O_2^-$ ($E = -0.33$ eV)[63] and Cr(VI)/Cr(II) ($E = 0.51$ eV),[64] the VB potential of $MnIn_2S_4$ is more negative than that of $H_2O/^{\cdot}$OH ($E = 2.4$ eV).[65] In this case, the catalyst cannot only reduce Cr(VI) to Cr(III), but also cannot generate $^{\cdot}O_2^-$ and $^{\cdot}$OH in the reaction system, which is contrary to the experimental results (NBT and TA detection test). Therefore, the electron transmission in α-MnO_2@$MnIn_2S_4$ is a novel Z-scheme mechanism instead of the traditional type-II mechanism.

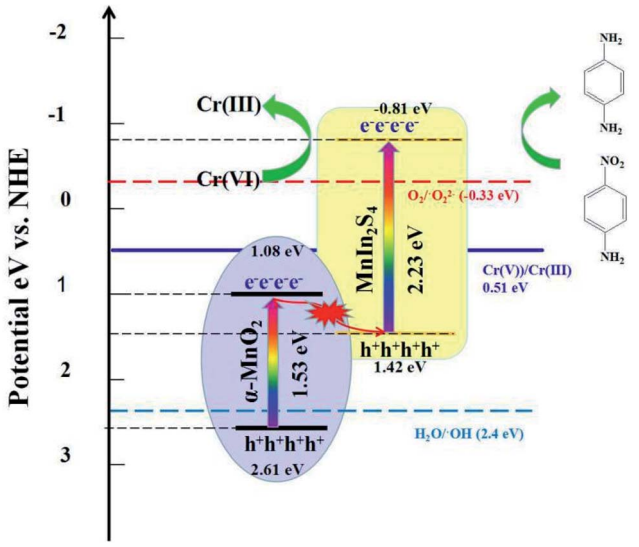

Fig. 12 Schematic illustration of the photocatalytic mechanism of α-MnO_2@$MnIn_2S_4$.

4 Conclusions

In summary, a core–shell α-MnO_2@$MnIn_2S_4$ hierarchical cubic Z-scheme heterostructure was designed and assembled by growing $MnIn_2S_4$ nanosheets *in situ* on the surface of α-MnO_2 nanocubes as a heterojunction photocatalyst, which was used to efficiently reduce 4-NA and Cr(VI) under visible light. The composition and structure of the final heterojunction were controlled by facile annealing treatment and a hydrothermal reaction. The interface contact heterojunction defined at the atomic-level has proven the effective and rapid migration of photogenerated carriers on the catalytic surface, and the complex multilayer structure also exposes abundant catalytic sites, providing a large specific surface area for the adsorption of 4-NA and Cr(VI), and consequently, highly improving the photocatalytic reduction reaction. As a result, Z-scheme α-MnO_2@$MnIn_2S_4$ with the optimal composition ratio showed excellent reduction performance and cycle stability. The selective reduction of 4-NA to 4-PDA was almost complete (99.6%) within 90 minutes, and the Cr(VI) reduction efficiency reached more than 93% within 120 minutes. This work reveals the basis of the photocatalytic performance of α-MnO_2@$MnIn_2S_4$ composite materials and has potential application in organic photosynthesis and pollutant purification.

Credit author statement

Min Zhang: Conceptualization, methodology, software, investigation, and writing-original draft. Muhammad Arif and

Yuxiang Hua: Writing – review & editing, supervision, and visualization. Bo Qiu: Resources, software, supervision, and data curation. Yue Mao: Resources and visualization. Xiaoheng Liu: Writing-review & editing and supervision. All the authors discussed the results and commented on the article.

Conflicts of interest

There are no conflicts to declare.

Acknowledgements

This work was supported by the National Natural Science Foundation of China (51872141). The TEM part of this work was supported by Mr Chenyao Hu from Nanjing Forestry University.

References

1 D. A. Nicewicz and D. W. C. MacMillan, *Science*, 2008, **322**, 77–80.
2 H. Seo, M. H. Katcher and T. F. Jamison, *Nat. Chem.*, 2017, **9**, 453–456.
3 H. B. Yu, L. B. Jiang, H. Wang, B. B. Huang, X. Z. Yuan, J. H. Huang, J. Zhang and G. M. Zeng, *Small*, 2019, **15**, 1901008.
4 B. Weng, S. Q. Liu, N. Zhang, Z. R. Tang and Y. J. Xu, *J. Catal.*, 2014, **309**, 146–155.
5 R. W. Liang, F. F. Jing, G. Y. Yan and L. Wu, *Appl. Catal., B*, 2017, **218**, 452–459.
6 A. L. Chibac, V. Melinte, V. Brezová, E. A. Brosseau, V. Langlois and D. L. Versace, *ChemCatChem*, 2019, **11**, 3307–3317.
7 K. Mishra, T. N. Poudel, N. Basavegowda and T. R. Lee, *J. Catal.*, 2016, **344**, 273–285.
8 Z. H. Farooqi, R. Khalid, R. Begum, U. Farooq, Q. S. Wu, W. T. Wu, M. Ajamal, A. Irfan and K. Naseem, *Environ. Technol.*, 2019, **40**, 2027–2036.
9 M. A. Pandit, S. H. K. N. Dasari, S. Billakanti, M. Ramadoss and K. Muralidharan, *J. Phys. Chem. C*, 2020, **124**, 18010–18019.
10 T. Liu, Y. Sun, B. Jiang, W. Guo, W. Qin, Y. M. Xie, B. Zhao, L. Zhao, Z. Q. Liang and L. Jiang, *ACS Appl. Mater. Interfaces*, 2020, **12**, 28100–28109.
11 W. Chen, T. Y. Liu, T. Huang, X. H. Liu and X. J. Yang, *Nanoscale*, 2016, **8**, 3711–3719.
12 P. Viswanathan and R. Ramaraj, *J. Mol. Catal. A: Chem.*, 2016, **424**, 128–134.
13 M. Misra, S. R. Chowdhury and T. I. Lee, *Appl. Catal., B*, 2020, **272**, 118991.
14 L. Hou, Y. Q. Zhang, Y. Y. Ma, Y. L. Wang, Z. F. Hu, Y. Z. Gao and Z. G. Han, *Inorg. Chem.*, 2019, **58**, 16667–16675.
15 B. Jiang, Y. F. Gong, J. N. Gao, T. Sun, Y. J. Liu, N. Oturan and M. A. Oturan, *J. Hazard. Mater.*, 2019, **365**, 205–226.
16 J. Ding, L. T. Pu, Y. F. Wang, B. D. Wu, A. Q. Yu, X. L. Zhang, B. C. Pan, Q. X. Zhang and G. D. Gao, *Environ. Sci. Technol.*, 2018, **52**, 12602–12611.
17 H. L. Ma, Y. M. Zhang, Q. H. Hu, D. Yan, Z. Z. Yu and M. L. Zhai, *J. Mater. Chem.*, 2012, **22**, 5914–5916.
18 X. Zheng, D. Yuan, Y. Li and C. G. liu, *Environ. Pollut.*, 2019, **254**, 113042.
19 C. P. Xu, P. R. Anusuyadevi, C. Aymonier, R. Luque and S. Marre, *Chem. Soc. Rev.*, 2019, **48**, 3868–3902.
20 L. Buzzetti, G. E. M. Crisenza and P. Melchiorre, *Angew. Chem., Int. Ed.*, 2019, **58**, 3730–3747.
21 A. Li, W. Zhu, C. C. Li, T. Wang and J. L. Gong, *Chem. Soc. Rev.*, 2019, **48**, 1874–1907.
22 R. Xiao, C. X. Zhao, Z. Y. Zou, Z. P. Chen, L. Tian, H. T. Xu, H. Tang, Q. Q. Liu, Z. X. Lin and X. F. Yang, *Appl. Catal., B*, 2020, **268**, 118382.
23 H. H. Zeng, B. L. Xing, C. T. Zhang, L. J. Chen, H. H. Zhao, X. F. Han, G. Y. Yi and G. X. Huang, *Energy Fuels*, 2020, **34**, 2480–2491.
24 S. I. Han, S. W. Lee, M. G. Cho, J. M. Yoo, M. H. Oh, B. Jeong, D. Kim, O. K. Park, J. C. Kim, E. Namkoong, J. W. Jo, N. Lee, C. H. Lim, M. Soh, Y. E. Sung, J. M. Yoo, K. Park and T. W. Hyeon, *Adv. Mater.*, 2020, **32**, 2001566.
25 X. Sun, G. L. Zhang, R. H. Du, R. Xu, D. W. Zhu, J. C. Qian, G. Bai, C. Yang, Z. Y. Zhang, X. Zhang, D. H. Zou and Z. Y. Wu, *Biomaterials*, 2019, **194**, 151–160.
26 P. Miao, J. X. Chen, Y. S. Tang, K. J. Chen and J. Kong, *Sci. China Mater.*, 2020, 1–12.
27 D. L. Chao, C. Ye, F. X. Xie, W. H. Zhou, Q. H. Zhang, Q. F. Gu, K. Davey, L. Gu and S. Z. Qiao, *Adv. Mater.*, 2020, **32**, 2001894.
28 F. W. Boyom-Tatchemo, F. Devred, G. Ndiffo-Yemeli, S. Laminsi and E. M. Gaigneaux, *Appl. Catal., B*, 2020, **260**, 118159.
29 Y. G. Zhang, M. Y. Wu, Y. H. Kwok, Y. F. Wang, W. Zhao, X. L. Zhao, H. B. Huang and D. Y. C. Leung, *Appl. Catal., B*, 2019, **259**, 118034.
30 P. Wu, S. Q. Dai, G. X. Chen, S. Q. Zhao, M. L. Fu, P. R. Chen, Q. Chen, X. J. Jin, Y. C. Qiu, S. H. Yang and D. Q. Ye, *Appl. Catal., B*, 2020, **268**, 118418.
31 S. B. Wang, Y. Wang, S. L. Zhang, S. Q. Zang and X. W. Lou, *Adv. Mater.*, 2019, **31**, 1903404.
32 C. Y. Liu, X. Li, J. Z. Li, Y. J. Zhou, L. L. Sun, H. Q. Wang, P. W. Huo, C. C. Ma and Y. S. Yan, *Carbon*, 2019, **152**, 565–574.
33 D. Santamaria-Perez, M. Amboage, F. J. Manjon, D. Errandonea, A. Muñoz, P. Rodríguez-Hernández, A. Mújica, S. Radescu, V. V. Ursaki and I. M. Tiginyanu, *J. Phys. Chem. C*, 2012, **116**, 14078–14087.
34 W. Chen, Z. C. He, G. B. Huang, C. L. Wu, W. F. Chen and X. H. Liu, *Chem.Eng. J.*, 2019, **359**, 244–253.
35 X. Q. Chen, Z. G. Cao, L. D. Xing, Y. H. Liao, Y. C. Qiu and W. S. Li, *Nanoscale*, 2017, **9**, 18467–18473.
36 H. Zhang, Q. Qi, P. G. Zhang, W. Zheng, J. Chen, A. G. Zhou, W. B. Tian, W. Zhang and Z. M. Sun, *ACS Appl. Energy Mater.*, 2018, **2**, 705–714.
37 H. Fang and P. Jena, *J. Mater. Chem. A*, 2016, **4**, 4728–4737.
38 W. Wang and L. Ao, *Cryst. Growth Des.*, 2008, **8**, 358–362.
39 B. K. Wu, G. B. Zhang, M. Y. Yan, T. F. Xiong, P. He, L. he, X. Xu and L. Q. Mai, *Small*, 2018, **14**, 1703850.

40 Y. Shiraishi, J. Imai, N. Yasumoto, H. Sakamoto, S. Tanaka, S. Ichikawa and T. Hira, *Langmuir*, 2019, **35**, 5455–5462.
41 C. K. Yao, A. L. Yuan, Z. S. Wang, H. Lei, L. Zhang, L. M. Guo and X. P. Dong, *J. Mater. Chem. A*, 2019, **7**, 13071–13079.
42 R. Bi, G. X. Liu, C. Zeng, X. P. Wang, L. Zhang and S. Z. Qiao, *Small*, 2019, **15**, 1804958.
43 B. X. Li, G. X. Rong, Y. Xie, L. F. Huang and C. Q. Feng, *Inorg. Chem.*, 2006, **45**, 6404–6410.
44 H. Chen, M. Q. Wang, Y. N. Yu, H. Liu, S. Y. Lu, S. J. Bao and M. W. Xu, *ACS Appl. Mater. Interfaces*, 2017, **9**, 35040–35047.
45 C. Revathi and R. T. R. Kumar, *Electroanalysis*, 2017, **29**, 1481–1489.
46 L. B. Ni, Z. Wu, G. L. Zhao, C. Y. Sun, C. Q. Zhou, X. X. Gong and G. W. Diao, *Small*, 2017, **13**, 1603466.
47 D. L. Chao, W. H. Zhou, C. Ye, Q. H. Zhang, Y. G. Cheng, L. Gu, K. Davey and S. Z. Qiao, *Angew. Chem., Int. Ed.*, 2019, **58**, 7823–7828.
48 X. Shi, H. Zheng, A. M. Kannan, P. Salcedo and B. Escobar, *Inorg. Chem.*, 2019, **58**(8), 5335–5344.
49 M. Zhang, J. C. Yao, M. Arif, B. Qiu, H. F. Yin, X. H Liu and S. M. Chen, *Appl. Surf. Sci.*, 2020, **526**, 145749.
50 Y. Y. Shi, S. M. Gao, Y. F. Yuan, G. J. Liu, R. C. Jin, Q. Y. Wang, H. Xu and J. Lu, *Nano Energy*, 2020, **77**, 105153.
51 Y. Chen, X. Zhang, C. Xu and H. Xu, *Electrochim. Acta*, 2019, **309**, 424–431.
52 R. Sha, N. Vishnu and S. Badhulika, *Sens. Actuators, B*, 2019, **279**, 53–60.
53 C. X. Zhao, L. Tian, Z. Y. Zou, Z. P. Chen, H. Tang, Q. Q. Liu, Z. X. Lin and X. F. Yang, *Appl. Catal., B*, 2020, **268**, 118445.
54 Y. C. Zhang, N. Afzal, L. Pan, X. W. Zhang and J. J. Zou, *Adv. Sci.*, 2019, **6**, 1900053.
55 J. Zhou, J. X. Cui, M. Dong, C. Y. Sun, S. Q. You, X. L. Wang, Z. Y. Zhou and Z. M. Su, *Chem. Commun.*, 2020, **56**, 7261–7264.
56 S. M. Ghoreishian, K. S. Ranjith, H. Lee, H. I. Ju, S. Z. Nikoo, Y. K. Han and Y. S. Huh, *J. Hazard. Mater.*, 2020, **391**, 122249.
57 L. H. Zheng, H. R. Su, J. Z. Zhang, L. S. Walekar, B. X. Zhou, M. C. Long and Y. H. Hu, *Appl. Catal., B*, 2018, **239**, 475–484.
58 M. M. Fang, J. X. Shao, X. G. Huang, J. Y. Wang and W. Chen, *J. Mater. Sci. Technol.*, 2020, **56**, 133–142.
59 P. J. Li, W. Cao, Y. Zhu, Q. Y. Teng, L. Peng, C. Y. Jiang, C. S. Feng and Y. P. Wang, *Sci. Total Environ.*, 2020, **715**, 136809.
60 H. F. Yin, Y. Cao, T. L. Fan, M. Zhang, J. C. Yao, P. F. Li, S. M. Cheng and X. H. Liu, *Sci. Total Environ.*, 2020, **754**, 141926.
61 Y. C. Deng, J. Liu, Y. B. Huang, M. M. Ma, K. Liu, X. M. Dou, Z. J. Wang, S. C. Qu and Z. G. Wang, *Adv. Funct. Mater.*, 2020, **30**, 2002353.
62 M. Li, H. W. Huang, S. X. N. Tian and Y. H. Zhang, *ChemCatChem*, 2018, **10**, 4477–4496.
63 T. Huang, Y. T. Luo, W. Chen, J. C. Yao and X. H. Liu, *ACS Sustainable Chem. Eng.*, 2018, **6**, 4671–4679.
64 C. Cheng, D. Y. Chen, N. J. Li, Q. F. Xu, H. Li, J. H. he and J. M. Lu, *J. Hazard. Mater.*, 2020, **391**, 122205.
65 W. Chen, L. Chang, S. B. Ren, Z. C. He, G. B. Huang and X. H. Liu, *J. Hazard. Mater.*, 2020, **384**, 121308.